DOI: 10.24874/ti.2364.09.26.11

Tribology in Industry

www.tribology.rs

RESEARCH

Analysis of Wear Behavior Combined with Mechanical Properties and Wear Track Geometries of AlCrTiSiN and TiAlSiN PVD Coatings on SKD61 Tool Steel

Yupin Supachoke[a], Sutham Siwawut[b,*]

[a]*Department of Engineering, Faculty of Engineering, Rajamangala University of Technology Krungthep, Bangkok, 10120, Thailand,*
[b]*Department of Industrial Engineering, Faculty of Engineering, Rajamangala University of Technology Krungthep, Bangkok, 10120, Thailand.*

Keywords:

Mechanical properties
Adhesion
Filtered cathodic arc plasma
Wear track
Specific wear rate

* Corresponding author:

Sutham Siwawut
E-mail: sutham.s@mail.rmutk.ac.th

Received: 25 September 2026
Revised: 27 October 2026
Accepted: 12 November 2026

A B S T R A C T

The aim of this research is to study the wear behavior of PVD hard coatings by assessing the tribological performance, adhesion strength, and wear resistance of AlCrTiSiN and TiAlSiN coatings deposited on SKD61 steel, using geometrical wear-track profiling and microstructural analyses to clarify the failure process. The test results showed that the AlCrTiSiN coating exhibited a smoother surface, higher hardness, and better adhesion strength than the TiAlSiN coating. Conversely, geometric analysis of the wear tracks to calculate specific wear rates revealed that the TiAlSiN coating exhibited a lower wear rate than the AlCrTiSiN coating. Examination of the wear track profiles and high-magnification images showed that the AlCrTiSiN track featured a conformal circular-arc profile—characteristic of continuous abrasive wear. In contrast, the TiAlSiN wear track was unusually narrow with steep walls; this morphology resulted from severe failure—specifically coating delamination and interfacial flaking—rather than standard abrasive wear, leading to an anomalous volume loss.

© 2026 Published by Faculty of Engineering

Article in Press

1. INTRODUCTION

In industry, cutting tools and dies continuously encounter severe operating conditions, including extreme mechanical loads, high temperatures, and intense friction, that lead to rapid wear and reduced tool life [1,2]. To deal with these issues, researchers have extensively studied Physical Vapor Deposition (PVD) hard coatings to enhance the tribological performance and extend the service life of tool steels, particularly SKD61 [3,4]. One widely used PVD technique for producing thin films is Cathodic Arc Plasma Deposition (CAPD) because of its highly dense and adherent ionized, energetic plasma [5-16]. However, during this deposition, molten macroparticles are emitted onto the substrate,

increasing surface roughness and initiating micro-cracks [13]. Later, a filter was used to eliminate macroparticles, known as Filtered Cathodic Vacuum Arc (FCVA) systems [14-16].

Although FCVA can resolve surface defect issues, the coating's mechanical properties remain critical to tool life. TiN and TiAlN coatings were widely used because they offer significantly higher hardness and superior oxidation resistance compared with bare steel substrates, which are no longer sufficient [17,18]. This has driven the development of nanocomposite coatings by adding silicon [19,20] and chromium [21,22]. For instance, Si-doped TiAlN coatings involve the formation of an amorphous SiN_x phase within the nanocrystalline (Ti, Al) N structure [19,20,23-25]. According to Veprek's theory [26], this architecture originates from the thermodynamic phase segregation of nanocrystalline (nc-) (Ti, Al) N phases embedded in an amorphous a-Si_3N_4 matrix. This grain-boundary structure effectively impedes dislocation motion, resulting in TiAlSiN coating with superhardness and excellent thermal stability [27-30]. However, excessive Si content (>7.9 at. %) may degrade mechanical properties [31]. Despite the outstanding mechanical performance of TiAlSiN, its main limitations under high and prolonged compressive loads remain its brittleness and delamination [32,33]. Moreover, high hardness often comes with elevated residual stress, which weakens adhesion and can lead to fracture [34,35].

To resolve these limitations, adding chromium to the system greatly reduces residual stress in the coating compared to TiAlN-based systems [36,37]. Microstructurally, AlCrTiSiN coatings typically consist of face-centered cubic (fcc) nanocrystalline solid-solution phases embedded inside a dense amorphous Si_3N_4 matrix, reinforced by ultra-hard Cr_2N nanoprecipitates that impede plastic deformation [31,37-40]. The combination of Cr-induced solid-solution strengthening and a Si-based nanocomposite provides high stiffness, superior structural strength, and enhanced fracture resistance in comparison with conventional Ti-Al-Si-N systems.

Despite extensive research on AlCrTiSiN and TiAlSiN coatings, evaluations of general tribological wear behavior often rely solely on quantitative measurements of material loss volume and specific wear rates—approaches that can lead to erroneous conclusions regarding wear resistance. This research aims to analyze wear behavior by correlating mechanical properties with wear track geometry and high-magnification imagery of PVD-deposited AlCrTiSiN and TiAlSiN coatings on SKD61 tool steel substrates. To account for variations in chemical composition, layer thickness, and surface topography between the two systems, the comparative analysis goes beyond basic compositional attribution, providing a robust framework to reliably decouple material removal mechanisms from structural failure.

2. MATERIAL AND METHOD

2.1 Materials preparation

Commercial JIS SKD61 tool steel (25 × 40 × 10 mm) was vacuum-quenched and tempered to achieve a uniform hardness of 54 ± 1 HRC. The samples were then mechanically ground using silicon carbide (SiC) abrasive papers of 600, 1,000, and 1,500 grit and subsequently polished with 0.05 μm α-Al_2O_3 to eliminate residual grinding scratches from the abrasive paper. The substrates were finally buffed using a SAPHIR 330 polishing system (ATM Qness, Mammelzen, Germany) at 300 rpm using a felt polishing cloth and distilled water.

2.2 Coating deposition

The SKD61 substrates were coated with AlCrTiSiN and TiAlSiN coatings synthesized using a Filtered Cathodic Arc Plasma Deposition (FCAPD) system equipped with magnetic macroparticle filters. The filtering arrangements and deposition configurations were kept identical for both coating systems. Before deposition, the substrates underwent ultrasonic degreasing in an alkaline detergent, subsequently rinsed in absolute ethanol for 15 minutes to eliminate surface contaminants. The deposition process took place at a base pressure of 5.0×10^{-3} Pa. The chamber temperature was maintained isothermally at 400 °C. First, an argon glow discharge plasma cleaning was performed at a working pressure of 2.0 Pa. This was followed by sputtering of the substrate with Cr plasma to remove native oxides and enhance interfacial adhesion. Thereafter, a thin CrN layer was deposited to provide a stress-alleviating gradient interlayer. The AlCrTiSiN or TiAlSiN coatings were then deposited using high-purity alloy cathodes under a reactive nitrogen atmosphere with an arc operating current

Article in Press

maintained at approximately 70 A and a total deposition duration of 1.30 h. The reactive nitrogen partial pressure was regulated at 1.5 Pa while negative DC substrate bias was held at 100 V.

2.3 Surface morphology, elemental composition, and thickness

The surface morphology and elemental composition were characterized using a scanning electron microscope equipped with energy-dispersive X-ray spectroscopy (SEM-EDS; Hitachi SU5000, Tokyo, Japan, and Oxford Instruments, Abingdon, UK). The EDS compositional point analysis was performed at an accelerating voltage of 15 kV. The mean surface roughness (S_a) was measured using a white light interferometer, and average values were obtained from five representative locations per sample.

The thin-film thickness was evaluated by cross-sectioning with a precision abrasive cutter and preparing the samples via cold mounting in epoxy resin. The mounted samples were then mechanically ground using successive grades of silicon carbide (SiC) abrasive papers from 240 to 2400 grit and finally fine-polished with a 3 μm diamond suspension. The cross-sectional microstructure and coating thicknesses were subsequently characterized using SEM, with each layer thickness determined by averaging from five different positions along the cross-section.

2.4 Mechanical and adhesion properties of the coatings

The hardness (H) and elastic modulus (E) were determined using a nanoindentation tester (NHT2, Anton Paar, Graz, Austria) equipped with a Berkovich diamond indenter. A maximum load of 10 mN was applied, with a dwell time of 10 s at the peak load. Nanoindentation and scratch tests were performed with three replicate measurements on dedicated specimens to determine statistical variability, which were distinct from the independent wear test specimens. The quantitative adhesion of the coatings was evaluated via scratch testing using a Revetest Scratch Tester (RST, Anton Paar, Peseux, Switzerland). A linearly increasing normal load from 0 to 150 N was applied using a Rockwell C diamond indenter with a 200 μm tip radius. The scratch length was set at 10 mm with a constant traversal speed of 10 mm/min, corresponding to a normal loading rate of 150 N/min. The critical loads (L_{c1}, L_{c2}, and L_{c3}) were determined by correlating abrupt shifts in acoustic emission (AE) signals and friction force with optical microscopy observation, where L_{c1} represents the onset of initial cohesive cracking events, L_{c2} denotes the onset of adhesive spallation, and L_{c3} corresponds to complete coating failure or substrate exposure.

Furthermore, the qualitative adhesion of the coatings was evaluated using the Rockwell C indentation test with a constant load of 1,471 N (150 kgf) to evaluate the failure modes and adhesion classes.

2.5 Tribological testing and wear behaviour analysis

Tribological properties were examined by conducting a linear reciprocating sliding wear test according with the ASTM G133 standard [41] under unlubricated conditions (25±2°C, 50±5%RH) using a tungsten carbide (WC) ball counterbody (Grade YG6 containing a 6% Co binder, 6 mm in diameter, with a hardness of 1500–1600 HV and a surface roughness $R_a <$ 0.05 μm) was used, employing a fresh, unused ball for each test under a constant normal load (F) of 10 N. The reciprocating motion followed a sinusoidal waveform with a stroke length of 10 mm (defined as the peak-to-peak distance between reversal points) and a constant mean sliding speed of 0.15 m/s, corresponding to a frequency of 7.5 Hz. To achieve total sliding distances (S) of 300, 400, and 500 m, the corresponding number of cycles and test durations were 15,000 cycles (2,000 s), 20,000 cycles (2,667 s), and 25,000 cycles (3,333 s), respectively. For each coating system, three parallel wear tests were conducted on a single large specimen, maintaining a lateral spacing of 10 mm between adjacent tracks to eliminate mechanical cross-interference and debris contamination. Post-test, the 3D surface topography and cross-sectional wear profile of the wear track were characterized using a 3D laser scanning confocal microscope (LSCM; Olympus OLS5000, Japan). The wear volume (V) was quantified using a 3D optical profilometer by measuring the cross-sectional area of the wear track at five evenly spaced locations along the scar. The average cross-sectional area was then multiplied by the total sliding distance (S of 300,

Article in Press

400, and 500 m, corresponding to the accumulated reciprocating pass lengths) to calculate the net wear volume. The reference baseline was established using the unworn flat surface adjacent to the track, with local anomalies such as edge pile-ups excluded during profile integration to ensure data precision. Volumetric wear (V) was calculated by multiplying the average wear-track cross-sectional area measured at five equidistant locations along the wear track. The specific wear rate (W_s) was subsequently calculated using Archard's wear equation (1) [42]:

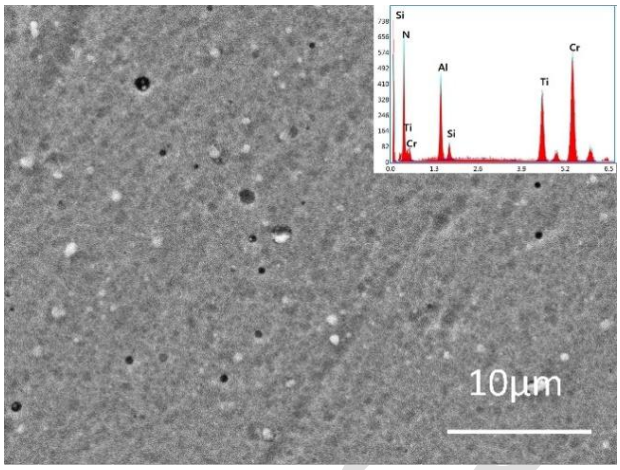
$$W_s = \frac{V}{F \times S} \quad (1)$$

3. RESULTS AND DISCUSSIONS

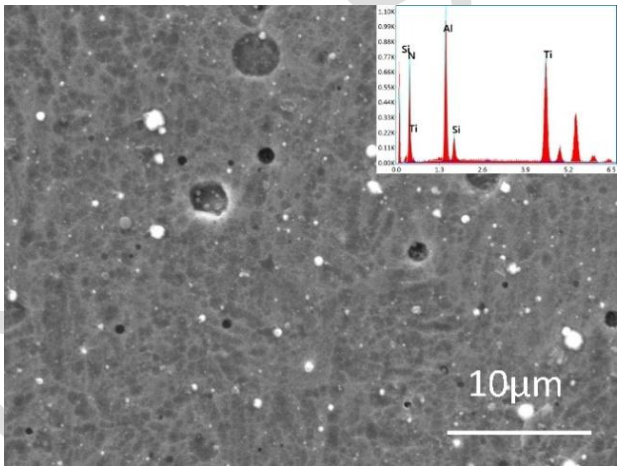
This section presents and discusses the experimental results of the AlCrTiSiN and TiAlSiN coatings deposited on SKD61 tool steel, focusing on their microstructural characteristics, mechanical properties, and tribological performance.

3.1 Microstructural Characterization

The pronounced morphological disparities in morphology between the two coatings in Fig. 1 show that the AlCrTiSiN coating in Fig. 1a displayed a relatively smooth, uniform surface with a S_a of 0.06 μm. While isolated micro-droplets were present, their density remained remarkably low. Conversely, the TiAlSiN coating in Fig. 1b showed deteriorated surface quality, characterized by numerous large macroparticles and surface craters, resulting in a S_a of 0.12 μm. Upon deposition, the surface roughness inevitably increased—a phenomenon inherent to Cathodic Arc Plasma Deposition due to the generation and incorporation of metallic macroparticles [15,16]. These macroparticles, ranging in size from 0.2 to 100 μm [12], strongly influence the final surface topography and the formation of eruption craters. Although the magnetic filter effectively removes the bulk of macroparticles under comparable processing conditions, trace residual micro-droplets can still occur due to localized target dynamics; consequently, the resulting variations in defect density primarily reflect the inherent evaporation characteristics and cathode alloy behavior of the respective targets.



(a)

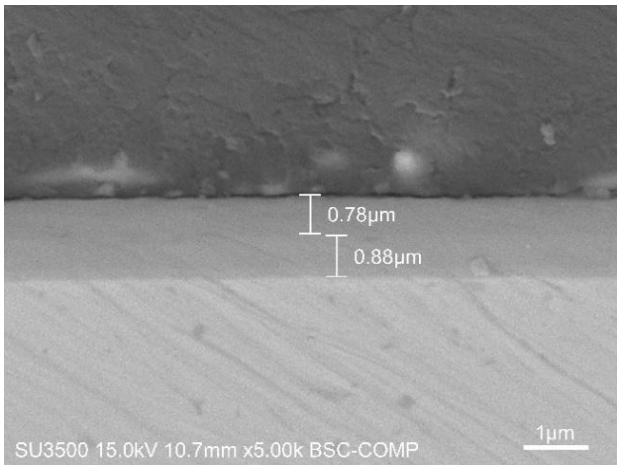


(b)

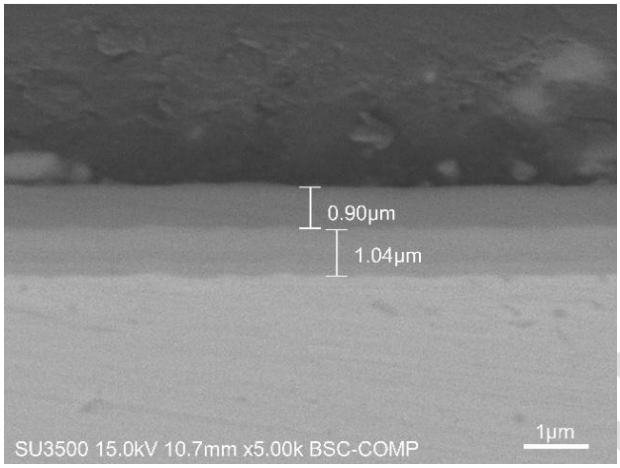
Fig. 1. SEM surface morphology of (a) AlCrTiSiN and (b) TiAlSiN coatings.

The elemental composition is presented in the inset of Fig. 1 and clearly exhibits the characteristic X-ray emission peaks of N, Al, Si, Ti, and Cr. Quantitative EDS measurements were conducted at an accelerating voltage of 15 kV, with data averaged from 5 distinct locations on each sample using a standardless quantification method. Substrate-related signals (such as Fe) were excluded, and the reported atomic percentages were normalized exclusively to the coating constituents. Based on quantitative EDS point analysis, the AlCrTiSiN coating in Fig. 1a consisted of 52.3 at.% N, 11.8 at.% Al, 2.1 at.% Si, 10.7 at.% Ti, and 23.1 at.% Cr, while the TiAlSiN coating in Fig.1b contained 58.2 at.% N, 19.6 at.% Al, 3.5 at.% Si, and 18.7 at.% Ti. Owing to the inherent limitations of light-element detection via EDS, the relatively high nitrogen content should be interpreted as a semi-quantitative compositional trend rather than an exact stoichiometric ratio.

Article in Press



(a)



(b)

Fig. 2. SEM cross-sectional of (a) AlCrTiSiN and (b) TiAlSiN coatings.

In the cross-sectional SEM micrographs presented in Fig. 2, the CrN interlayer and topcoat thicknesses of the AlCrTiSiN architecture in Fig. 2a are 0.88 μm and 0.78 μm, respectively. For the TiAlSiN in Fig. 2b, the CrN interlayer and topcoat thicknesses are 1.04 μm and 0.90 μm, respectively.

3.2 Mechanical Properties

The hardness of the AlCrTiSiN and TiAlSiN coatings was measured using nanoindentation. The maximum contact penetration depth was constrained to a small fraction of the coating thickness [43,44]. The measured experimental h_{max} values for the AlCrTiSiN and TiAlSiN coatings were found to be 116.45 nm and 118.17 nm, respectively. Fig. 3 presents representative load-displacement curves for the AlCrTiSiN and TiAlSiN coatings from nanoindentation testing, exhibiting the typical elastic-plastic deformation behavior of hard ceramic coatings under peak load. Owing to the multilayer architecture of the coating system—comprising the topcoat and a CrN interlayer—the indentation depths inherently reflect a partial mechanical contribution from the underlying interlayer. Consequently, the measured hardness and elastic modulus represent the effective composite properties of the coating architecture rather than purely intrinsic topcoat properties, whereas any direct influence from the SKD61 substrate remains negligible.

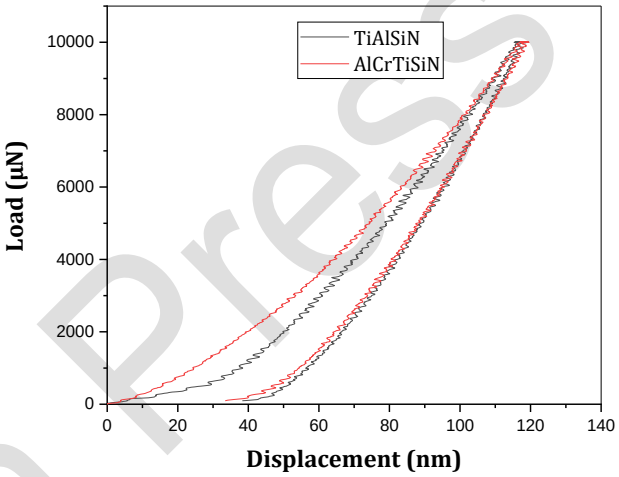


Fig. 3. Representative load-displacement curves of the AlCrTiSiN and TiAlSiN coatings.

As observed in Fig. 3, the loading curve of the AlCrTiSiN coating (red line) is shifted slightly to the left of the TiAlSiN coating (black line). This indicates that at any given applied load, the AlCrTiSiN coating exhibits a smaller indentation depth, reflecting its higher resistance to penetration and superior hardness. Furthermore, by evaluating the unloading curves and the residual indentation depth (h_f) upon complete load removal, the AlCrTiSiN coating shows a smaller residual depth of approximately 34 nm compared to approximately 40 nm for the TiAlSiN coating. This demonstrates that the AlCrTiSiN coating possesses enhanced elastic recovery and superior resistance to permanent plastic deformation.

The value of Poisson's ratio for the hard film was assumed to be 0.25 for the elastic modulus derived from the reduced modulus. The values of hardness and elastic modulus of the AlCrTiSiN coating are 34.24 ± 2.06 GPa and 399.94 ± 7.91 GPa, respectively. In contrast, the same properties of the TiAlSiN coating are 32.71 ± 2.67 GPa and 387.38 ± 8.34 GPa, respectively, and are lower. The value of elastic strain-to-failure of the AlCrTiSiN coating is 0.09, and that of TiAlSiN is

Article in Press

0.08. The plastic resistance index (H^3/E^2) of the AlCrTiSiN and TiAlSiN coatings is 0.25 GPa and 0.23 GPa, respectively.

The hardness enhancement of the AlCrTiSiN architecture is widely understood to arise from solid-solution strengthening by substitutional Cr atoms, along with differences in atomic radii, localized lattice strain, and grain-refinement strengthening [35,36,39,45,46]. According to the literature, the incorporation of Si typically promotes thermodynamically driven phase segregation, which is widely considered to result in a microstructure consisting of nanocrystalline nitride grains (nc-MeN) encapsulated by an interfacial tissue phase of an amorphous silicon nitride matrix (a-Si_3N_4). This biphasic phase boundary is expected to effectively restrict dislocation glide and grain boundary sliding [19, 24,26,27,30]. As shown by the results, the AlCrTiSiN coating shows a 4.7% increase in intrinsic hardness, and its resistance to plastic deformation also increases by 7.7% compared with TiAlSiN.

Figs. 4 and 5 show a quantitative scratch adhesion test under an optical microscope, detecting critical failure loads in conjunction with continuous AE monitoring [47]. The scratch tracks and AE signals of the AlCrTiSiN coating shown in Fig. 4a and 5a show the first appearance of a cohesive crack (L_{c1}) at a normal load of 40.65 ± 2.52 N, then edge chipping (L_{c2}) at 43.54 ± 2.25 N, and finally adhesive debonding (L_{c3}) at 97.59 ± 1.62 N. The TiAlSiN coating shows damage mechanisms and AE signal vibration earlier than the AlCrTiSiN coating in Fig. 4b and 5b, resulting in critical loads of L_{c1} of 15.22 ± 3.24 N, L_{c2} of 20.57± 2.97 N, and L_{c3} of 87.85 ± 2.48 N.

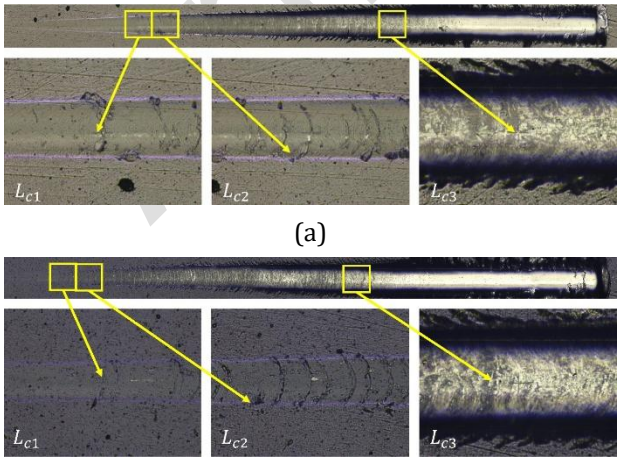


Fig. 4. Optical micrographs of the scratch test tracks of (a) AlCrTiSiN and (b) TiAlSiN coatings.

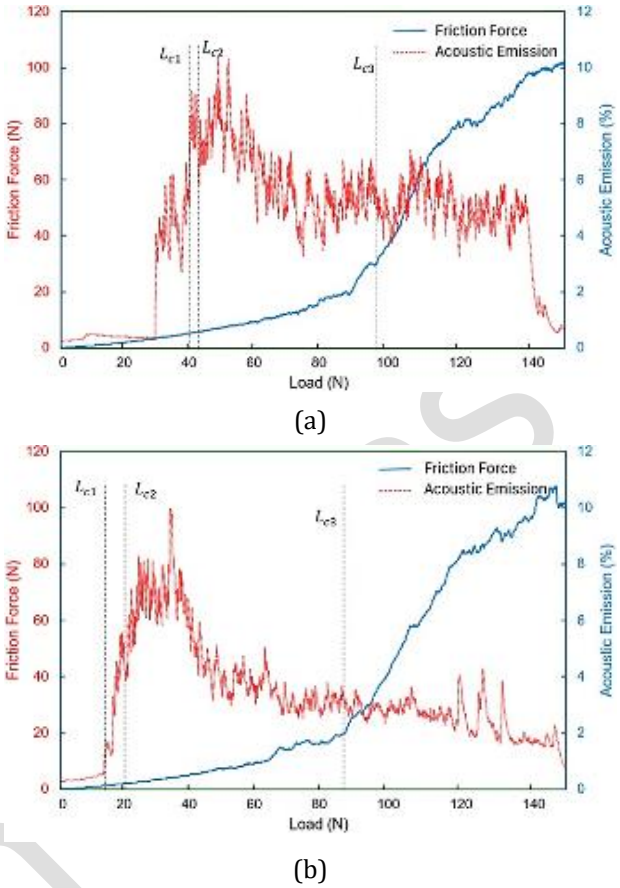


Fig. 5. Acoustic emission and friction force profiles versus applied load of (a) AlCrTiSiN and (b) TiAlSiN coatings.

The AlCrTiSiN coating shows stable friction-force behavior with low acoustic emission (AE) up to a normal load of 40.65 N. The rise in AE level and variation in friction force at this load suggest the initiation of cracks in cohesion, and hence the AlCrTiSiN coating is suggested to exhibit a superior critical load for crack initiation compared to the TiAlSiN coating. From the perspective of conventional thin-film behavior, increased hardness is frequently accompanied by heightened brittleness, which tends to induce premature cohesive microcracking at localized stress-concentration zones [6,28], implying that harder films are normally expected to show lower L_{c1} values. However, the AlCrTiSiN coating demonstrates an exceptionally high crack initiation load alongside its increased hardness, showing an improvement of over 160% relative to the TiAlSiN coating.

The qualitative adhesion assessment using SEM images for both the AlCrTiSiN and TiAlSiN coatings is shown in Fig. 6a and 6b, respectively.

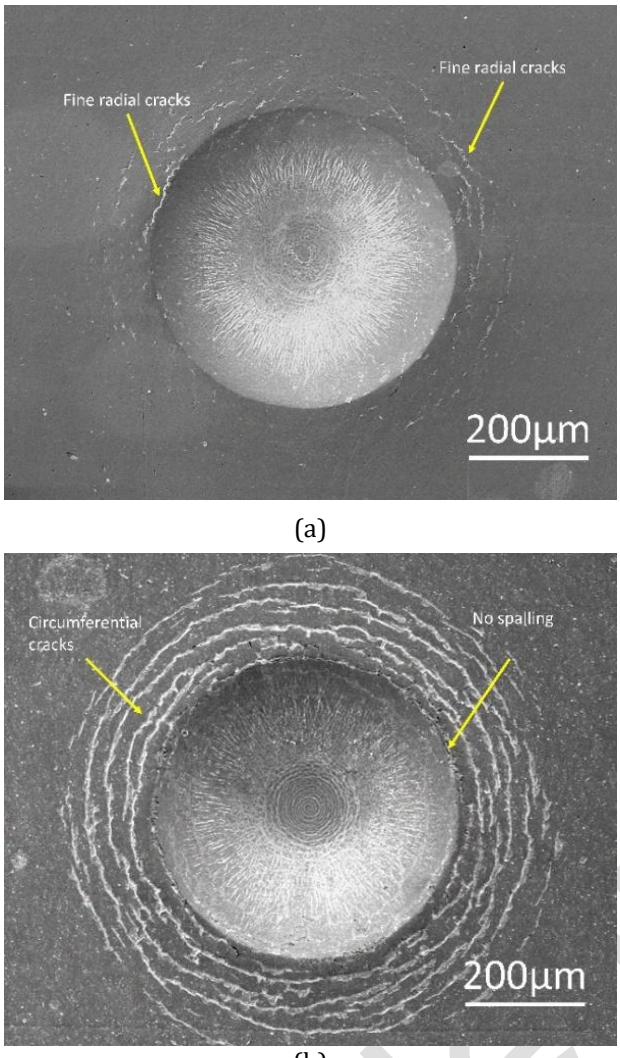


Fig. 6. Rockwell C indentation of (a) AlCrTiSiN and (b) TiAlSiN coatings.

The indentations on the AlCrTiSiN coating show only discrete, fine radial micro-cracks around the circumference, reflecting enhanced resistance to localized cracking in line with its elevated elastic strain-to-failure index (H/E) ratio and L_{c1}, supporting its adhesion class HF1. In comparison, the TiAlSiN coating shows numerous circumferential cracks; however, there is no evidence of extensive interfacial delamination or interfacial flaking, and it can be classified as HF2 according to the VDI 3198 standard failure criteria [48]. This property offers a perspective that contrasts with traditional concepts that require high Si content (5-7 at.%) to achieve optimal mechanical properties [19,26,27]. In this case, the moderate Si concentration (2.1-3.5 at.%) appears to help mitigate the classic embrittlement dilemma.

3.3 Tribological Properties

The friction data were subsequently smoothed using a moving-average filter with a window size of 20 points. In this signal-conditioning process, mechanical fluctuations are filtered out, yielding an accurate depiction of steady-state frictional behavior. Crucial comparisons between the raw and smoothed signals confirmed that the prominent fluctuations and transient peaks—which correspond directly to critical damage events such as micro-cracking, third-body debris entrapment, and localized coating breakdown—were fully preserved and not concealed by the filtering process. Fig. 7 shows the COF curve for the AlCrTiSiN and TiAlSiN coatings after a total sliding distance of 300 m.

During the initial run-in stage, the COF of the AlCrTiSiN coating rapidly increases within the first few meters and then transitions into the steady-state sliding regime with an average COF of ~0.22. Within the steady-state sliding interval (from 10 to 300 m), the AlCrTiSiN coating exhibits consistent frictional behavior, while the TiAlSiN coating maintains an average COF of ~0.57.

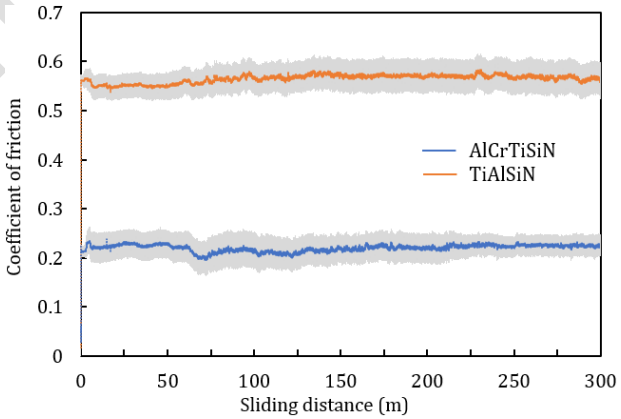


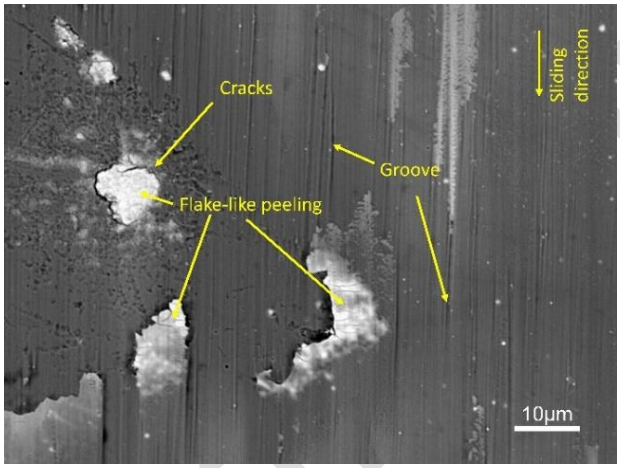
Fig. 7. COF for the AlCrTiSiN and TiAlSiN coatings.

This steady-state tribological response, with minimal dynamic fluctuation, is widely suggested in the literature to be potentially associated with the in-situ formation of passivating Cr_2O_3 and Al_2O_3 tribo-oxide films, owing to the high atomic fractions of Cr and Al, which prevent direct adhesive contact [6,45,49,50]. The SEM investigation of the AlCrTiSiN wear track at 300 m (Fig. 8a) shows a mostly intact contact area with parallel micro-striations produced by abrasion, along with tribo-films and micro-spalling, confirming a progressive, mild abrasive wear regime. At a total sliding distance of 500 m

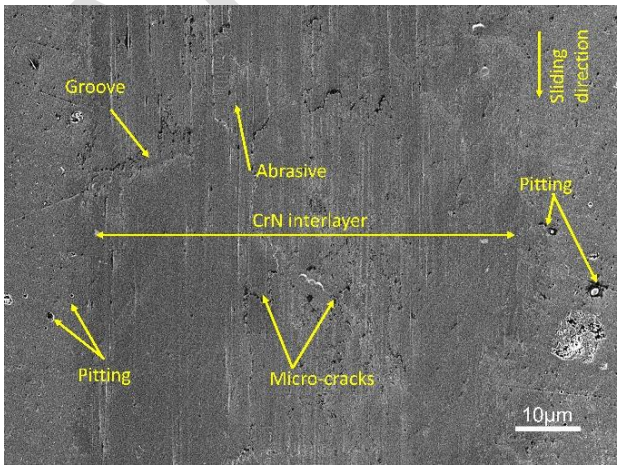
Article in Press

(Fig. 8b), the maximum wear depth reaches 0.84 μm, which exceeds the nominal topcoat thickness of 0.78 μm. This results in the exposure of the underlying CrN interlayer, accompanied by minor pitting and micro-cracking.

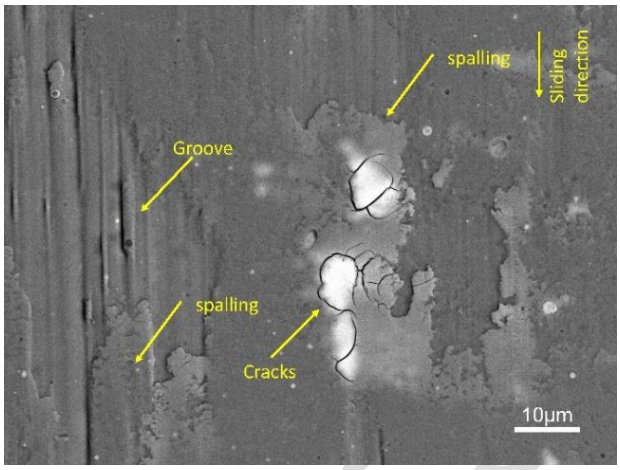
Conversely, the TiAlSiN coating exhibits a significantly higher COF throughout the sliding test. The SEM image at 300 m is presented in Fig. 8c. This image shows severe plowing grooves oriented in the direction of sliding, along with extensive micro-crack networks, droplet pull-out cavities, and spallation regions where catastrophic topcoat detachment occurs. At the sliding distance of 500 m (Fig. 8d), the maximum wear depth reaches 0.98 μm, surpassing the 0.90 μm topcoat thickness and leading to complete wear-through of the topcoat. The corresponding SEM micrograph reveals severe network micro-cracking, characteristic mud-crack patterns, and Hertzian ring cracks across the exposed CrN interlayer, indicating catastrophic brittle failure and extensive spallation.



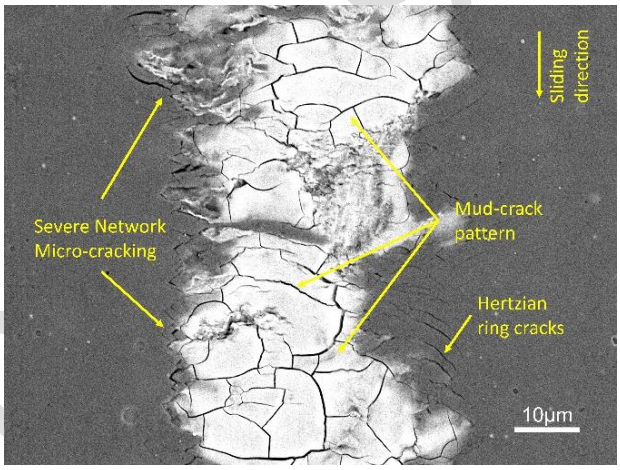
(a)



(b)



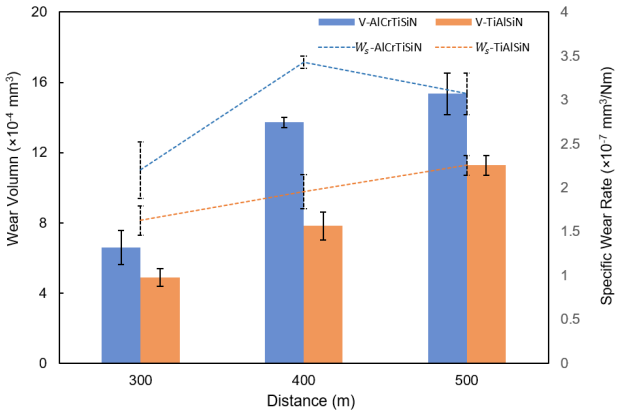
(c)



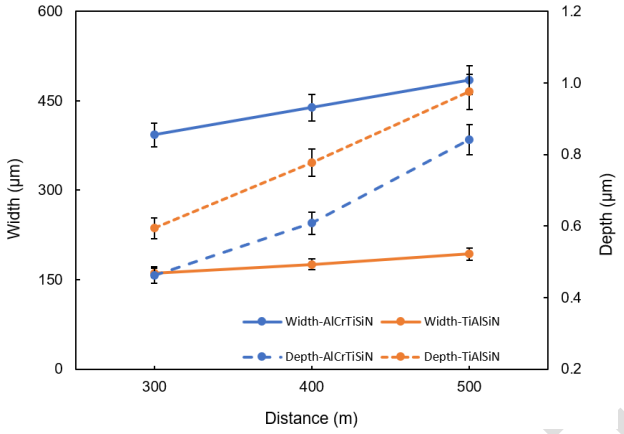
(d)

Fig. 8. SEM micrograph of the AlCrTiSiN at (a) 300m, (b) 500m, and TiAlSiN at (c) 300m, and (d) 500m.

Fig. 9a compares the wear volume and specific wear rate of the AlCrTiSiN and TiAlSiN coatings at sliding distances of 300, 400, and 500 m, with error bars representing the standard deviation derived from three independent replicate wear tests. The wear behaviour of the AlCrTiSiN coating shows an initial running-in increase, then reaches a steady state over prolonged sliding. The specific wear rate was 2.20×10^{-7} mm^3/Nm for 300 m, 3.43×10^{-7} mm^3/Nm for 400 m, and then dropped to 3.07×10^{-7} mm^3/Nm for 500 m. This subsequent decrease indicates a transition toward steady-state mild wear, resulting from tribo-chemical reactions within the real contact area that form a tribo-oxide layer. This layer acts as a solid lubricant film that reduces shear stress and suppresses severe adhesive wear [33,45,51]. This is shown by the wear volume behaviour, which showed pronounced early-stage accumulation between 300 and 400 m, increasing from 6.60 to 13.72×10^{-4} mm^3, and then increasing to only 15.34×10^{-4} mm^3 at 500 m.



(a)

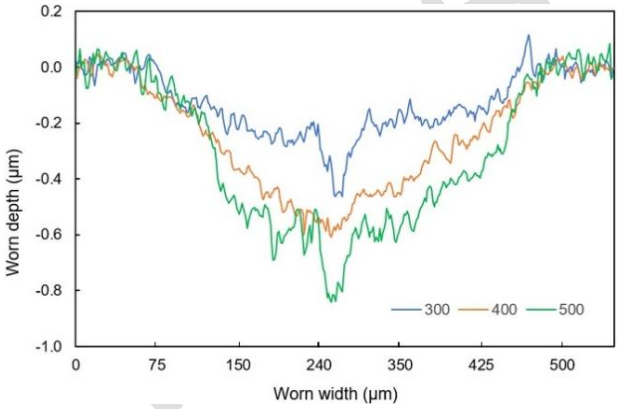


(b)

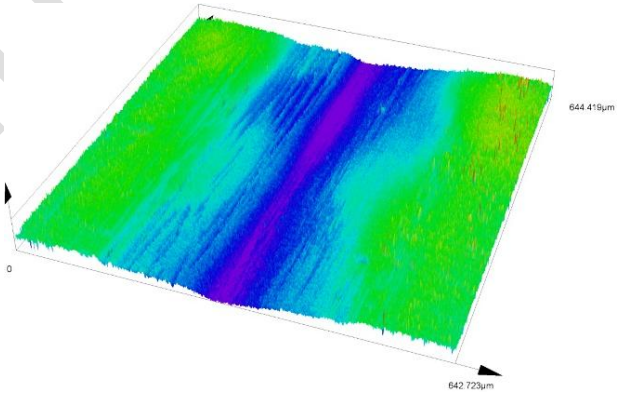
Fig. 9. Wear evolution of AlCrTiSiN and TiAlSiN coatings (a) Wear volume and specific wear rate (b) wear depth and width.

Similarly, the specific wear rate of the TiAlSiN coating increased continuously with increasing sliding distance, reaching 1.62, 1.96, and 2.26×10^{-7} mm^3/Nm at 300, 400, and 500 m, respectively. Meanwhile, the wear volume of the TiAlSiN coating increased from 4.88 to 7.82 and 11.28×10^{-4} mm^3 at 300, 400, and 500 m, respectively. Based on these quantitative profilometric data, an apparent tribological paradox emerges for the TiAlSiN coating, as it exhibited ostensibly lower volumetric loss and specific wear rate relative to the AlCrTiSiN coating. However, this ostensibly contradicts the aforementioned intrinsic mechanical properties of the mechanical profiles and plastic deformation resistance.

Evaluating tribological performance based solely on volumetric wear metrics can yield misleading conclusions; therefore, cross-sectional track dimensions were evaluated as shown in Figs. 9b, as the sliding distance increases, the maximum penetration depth of both coatings remains virtually identical. For the AlCrTiSiN coating, the wear depths at sliding distances of 300 m, 400 m, and 500 m were 0.46, 0.61, and 0.84 μm, respectively. Similarly, the corresponding wear depths for TiAlSiN coatings were 0.59, 0.78, and 0.98 μm, respectively. Nevertheless, the maximum wear-track width differed significantly between the two coatings and was twice that of the TiAlSiN coating. Specifically, the maximum width of the wear track for the AlCrTiSiN coating is 484.69 μm, while the width of the wear track for the TiAlSiN coating is 192.88 μm.



(a)

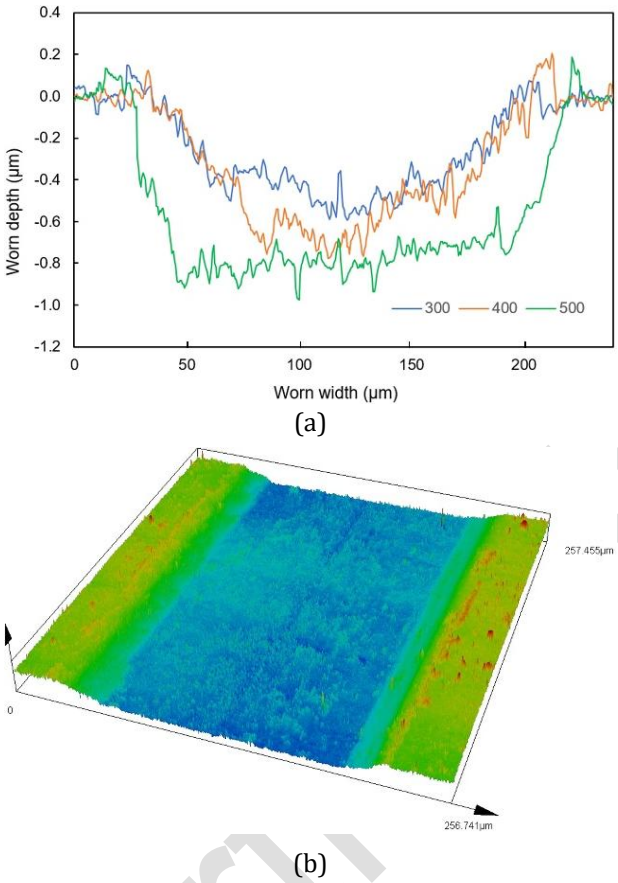


(b)

Fig. 10. Wear track of the AlCrTiSiN coating (a) 2D cross-sectional profile and (b) 3D surface topography.

Geometrical parameters of the wear track cross-sections in Fig. 10 reveal the distinct wear behavior of the AlCrTiSiN coating. Specifically, Fig. 10a shows 2D cross-sectional depth profiles at sliding distances of 300, 400, and 500 m, while Fig. 10b shows the 3D surface topography at the terminal 500 m sliding distance. The wear track of the coating exhibits an expanded width across all sliding distances. Notably, the measured track width significantly exceeds the theoretical chord width calculated from ideal static spherical indentation geometry (e.g., ~142 μm for a 3 mm radius ball at a depth of 0.84 μm). This substantial

dimensional discrepancy arises because the reciprocating sliding test operates under dynamic contact conditions rather than static equilibrium. As sliding progresses up to 500 m, the WC counterbody ball itself undergoes progressive wear and flattening (counterbody wear), continuously enlarging the active contact area. Furthermore, macro-scale sliding kinematics, frictional shear stresses, and reciprocating stroke dynamics drive lateral material removal well beyond the initial static spherical footprint.



(a)

(b)

Fig. 11. Wear track of the TiAlSiN coating (a) 2D cross-sectional profile and (b) 3D surface topography.

This profile of gradual, mild abrasive wear indicates that the coating has physical robustness and fracture toughness [28,35]. In contrast, the TiAlSiN coating in Fig. 11a exhibits a 2D cross-sectional depth profile with shallow arc geometry at sliding distances of 300 and 400 m and manifests an abnormally narrow, steep-walled, rectangular-like cross-sectional groove at a sliding distance of 500 m. As corroborated by 3D surface topography in Fig. 11b, from a contact mechanics standpoint, a spherical counterbody penetrating to such an indentation depth must geometrically produce a substantially wider chord width. It is hypothesized that this irregular geometry implies that the material removal did not proceed through continuous abrasion. Instead, this rectangular trench formed because the coating is brittle and has an elevated compressive residual stress [47,52].

In the TiAlSiN coating, it is suggested that propagating cracks were arrested and deflected laterally at the tough CrN interlayer, driving extensive interfacial shear failure that appeared as catastrophic cohesive spalling and flake-like peeling of the topcoat. Consequently, the severely flattened counterbody contact and localized deep trench formation restricted the actual contact geometry, confining the applied load to the central worn zone and potentially leading to an underestimation of the true volumetric material loss. Notably, direct observations and quantitative wear measurements of the WC counterbody scar, as well as explicit chemical analyses of potential tribo-oxide layers, were not performed in this study; therefore, the exact contribution of dynamic counterbody evolution and in-situ oxide formation remains a plausible mechanism rather than an established finding. Accordingly, it is possible that the lower measured volumetric loss observed for the TiAlSiN coating reflects localized catastrophic trenching rather than genuine wear resistance. In contrast, the higher volumetric loss of the AlCrTiSiN coating stems from a broader, stable wear track governed by mild, uniform abrasion—highlighting its exceptional structural stability and robust resistance to catastrophic delamination. The high wear resistance of AlCrTiSiN is widely attributed to the inclusion of Cr in the Ti-Al-N lattice, which is expected to provide solid-solution strengthening. The size of the Cr atom (1.25Å) is less than that of Ti and Al; consequently, this substitution is presumed to induce lattice strain, creating a stress field that restricts dislocation slip and potentially increases the material's hardness [22,30,38,53,54]. It is important to note that the present tribological evaluations were conducted under controlled laboratory conditions, specifically dry sliding against a WC counterbody at room temperature under a single normal load. While these findings provide valuable baseline data for coating selection, they do not directly translate to performance in industrial machining, cutting, or hot-forming operations. Consequently, assertions regarding industrial performance and service life are strictly confined to the scope of this laboratory study, and further validation under targeted operational environments is recommended.

Article in Press

4. CONCLUSION

In the study, the failure mechanisms of the AlCrTiSiN and TiAlSiN coatings were investigated by assessing their tribological performance, adhesion strength, and wear resistance. The following conclusions were obtained:

- The AlCrTiSiN coating exhibits an outstanding hardness and plastic resistance index of 34.24 GPa and 0.25, respectively, without the brittleness typically associated with super-hard nitrides. This enables it to resist crack initiation up to a normal load of 40.65 N, which is significantly higher than that of the TiAlSiN coating.
- The inclusion of Cr in the AlCrTiSiN coating contributed to a very smooth surface (S_a = 0.06 μm) compared to the TiAlSiN coating. Consequently, owing to its superior topographical quality and the formation of a tribo-oxide film, the AlCrTiSiN coating exhibited consistent and stable frictional behavior.
- Although the TiAlSiN coating showed a lower measured volume loss, cross-sectional and topographical data reveal that this lower value stems from localized, catastrophic trenching and severe brittle spalling rather than genuine wear resistance. By contrast, the higher volume loss observed in the AlCrTiSiN coating is due to a wider wear track shaped by mild abrasive wear, highlighting its strong structural integrity and resistance to catastrophic delamination.

Declaration of Competing Interests

The authors declare no known competing financial interests or personal relationships that could have influenced the work reported in this paper.

REFERENCES

[1] A. Rizzo *et al.*, "The Critical Raw Materials in Cutting Tools for machining Applications: A review," *Materials*, vol. 13, no. 6, p. 1377, Mar. 2020, doi: 10.3390/ma13061377.

[2] K. Bobzin, "High-performance coatings for cutting tools," *CIRP Journal of Manufacturing Science and Technology*, vol. 18, pp. 1–9, Dec. 2016, doi: 10.1016/j.cirpj.2016.11.004.

[3] C. S. Kumar, S. K. Patel, and F. Fernandes, "Performance of Al2O3/TiC mixed ceramic inserts coated with TiAlSiN, WC/C and DLC thin solid films during hard turning of AISI 52100 steel," *Journal of Materials Research and Technology*, vol. 19, pp. 3380–3393, Jun. 2022, doi: 10.1016/j.jmrt.2022.06.092.

[4] K.-D. Bouzakis, N. Michailidis, G. Skordaris, E. Bouzakis, D. Biermann, and R. M'Saoubi, "Cutting with coated tools: Coating technologies, characterization methods and performance optimization," *CIRP Annals*, vol. 61, no. 2, pp. 703–723, Jan. 2012, doi: 10.1016/j.cirp.2012.05.006.

[5] A. Anders, "A brief modern history of cathodic arc coating," in *50 Years of Vacuum Coating Technology and the Growth of the Society of Vacuum Coaters*, D. M. Mattox and V. Harwood Mattox, Eds. Albuquerque, NM, USA: Society of Vacuum Coaters, 2007, ch. 16, pp. 120–131.

[6] J. Terrat and M. Hecq, "Nouvelles tendances en procédés magnétron et arc pour le dépôt de couches minces," 1999.

[7] A. Ul-Hamid, "The effect of deposition conditions on the properties of Zr-carbide, Zr-nitride and Zr-carbonitride coatings – a review," *Materials Advances*, vol. 1, no. 5, pp. 988–1011, Jan. 2020, doi: 10.1039/D0MA00232A.

[8] H. Randhawa, "Review of plasma-assisted deposition processes," *Thin Solid Films*, vol. 196, no. 2, pp. 329–349, Feb. 1991, doi: 10.1016/0040-6090(91)90377-A.

[9] M. Muhammed, M. Javidani, T. E. Sadrabadi, M. Heidari, T. Levasseur, and M. Jahazi, "A comprehensive review of Cathodic arc Evaporation Physical Vapour Deposition (CAE-PVD) coatings for enhanced tribological performance," *Coatings*, vol. 14, no. 3, p. 246, Feb. 2024, doi: 10.3390/coatings14030246.

[10] P. Martin and A. Bendavid "Review of the filtered vacuum arc process and materials deposition," *Thin Solid Films*, vol. 394, no. 1–2, pp. 1–14, Aug. 2001, doi: 10.1016/S0040-6090(01)01169-5.

[11] J. E. Greene, "Review Article: Tracing the recorded history of thin-film sputter deposition: From the 1800s to 2017," *Journal of Vacuum Science & Technology A*, vol. 35, no. 5, Sep. 2017, doi: 10.1116/1.4998940.

[12] D. Manova, J. W. Gerlach, and S. Mändl, "Thin film deposition using energetic ions," *Materials*, vol. 3, no. 8, pp. 4109–4141, Jul. 2010, doi: 10.3390/ma3084109.

[13] R. L. Boxman and S. Goldsmith, "Macroparticle contamination in cathodic arc coatings: generation, transport and control," *Surface and Coatings Technology*, vol. 52, no. 1, pp. 39–50, Mar. 1992, doi: 10.1016/0257-8972(92)90369-L.

Article in Press

[14] A. Anders, "Approaches to rid cathodic arc plasmas of macro- and nanoparticles: a review," *Surface and Coatings Technology*, vol. 120–121, pp. 319–330, Nov. 1999, doi: 10.1016/S0257-8972(99)00460-0.

[15] A. Roy, S. Wang, and K. Komvopoulos, "A review of plasma-assisted deposition methods for amorphous carbon thin and ultrathin films with a focus on the cathodic vacuum arc technique," *Journal of Materials Research*, vol. 38, no. 3, pp. 586–616, Jan. 2023, doi: 10.1557/s43578-022-00868-9.

[16] Q. Hou *et al.*, "Thick tetrahedral amorphous carbon films deposited by filtered cathodic vacuum Arc," *Coatings*, vol. 15, no. 2, p. 241, Feb. 2025, doi: 10.3390/coatings15020241.

[17] S. PalDey and S. C. Deevi, "Single layer and multilayer wear resistant coatings of (Ti,Al)N: a review," *Materials Science and Engineering A*, vol. 342, no. 1–2, pp. 58–79, Dec. 2002, doi: 10.1016/S0921-5093(02)00259-9.

[18] P. H. Mayrhofer, C. Mitterer, L. Hultman, and H. Clemens, "Microstructural design of hard coatings," *Progress in Materials Science*, vol. 51, no. 8, pp. 1032–1114, Apr. 2006, doi: 10.1016/j.pmatsci.2006.02.002.

[19] S. Veprek, H. -d. Männling, M. Jilek, and P. Holubar, "Avoiding the high-temperature decomposition and softening of (Al1−xTix)N coatings by the formation of stable superhard nc-(Al1−xTix)N/a-Si3N4 nanocomposite," *Materials Science and Engineering A*, vol. 366, no. 1, pp. 202–205, Nov. 2003, doi: 10.1016/j.msea.2003.08.052.

[20] X. Wang *et al.*, "Review on tribological and corrosion properties of amorphous Silicon-Based coatings fabricated by chemical vapor deposition," *Coatings*, vol. 15, no. 9, p. 1016, Sep. 2025, doi: 10.3390/coatings15091016.

[21] S. Ganeshkumar *et al.*, "Performance of Multilayered Nanocoated Cutting Tools in High-Speed Machining: A review," *International Journal of Photoenergy*, vol. 2022, pp. 1–8, Oct. 2022, doi: 10.1155/2022/5996061.

[22] Y.-H. Hwang, K.-J. Seo, T.-H. Kim, Y. J. Min, Y. Liu, and D.-E. Kim, "Tribological behavior of TiN, AlTiN, and AlTiCrN coatings in atmospheric and vacuum environments," *Friction*, vol. 12, no. 11, pp. 2611–2626, Aug. 2024, doi: 10.1007/s40544-024-0930-3.

[23] L. Chen, Y. Du, A. J. Wang, S. Q. Wang, and S. Z. Zhou, "Effect of Al content on microstructure and mechanical properties of Ti–Al–Si–N nanocomposite coatings," *International Journal of Refractory Metals and Hard Materials*, vol. 27, no. 4, pp. 718–721, Dec. 2008, doi: 10.1016/j.ijrmhm.2008.12.002.

[24] Z.-W. Xie, L.-P. Wang, X.-F. Wang, L. Huang, Y. Lu, and J.-C. Yan, "Influence of Si content on structure and mechanical properties of TiAlSiN coatings deposited by multi-plasma immersion ion implantation and deposition," *Transactions of Nonferrous Metals Society of China*, vol. 21, pp. s476–s482, Aug. 2011, doi: 10.1016/S1003-6326(11)61628-2.

[25] B. Kucharska *et al.*, "Comparison study of PVD coatings: TIN/ALTIN, TIN and TIALSIN used in wood machining," *Materials*, vol. 15, no. 20, p. 7159, Oct. 2022, doi: 10.3390/ma15207159.

[26] S. Vepřek and S. Reiprich, "A concept for the design of novel superhard coatings," *Thin Solid Films*, vol. 268, no. 1–2, pp. 64–71, Nov. 1995, doi: 10.1016/0040-6090(95)06695-0.

[27] S. Veprek, M. G. J. Veprek-Heijman, P. Karvankova, and J. Prochazka, "Different approaches to superhard coatings and nanocomposites," *Thin Solid Films*, vol. 476, no. 1, pp. 1–29, Dec. 2004, doi: 10.1016/j.tsf.2004.10.053.

[28] S. K. Mishra, "Toughening of nanocomposite hard coatings," *Reviews on Advanced Materials Science*, vol. 59, no. 1, pp. 553–585, Jan. 2020, doi: 10.1515/rams-2020-0049.

[29] Y.-Y. Chang and S.-M. Yang, "High temperature oxidation behavior of multicomponent TiAlSiN coatings," *Thin Solid Films*, vol. 518, no. 21, pp. S34–S37, Mar. 2010, doi: 10.1016/j.tsf.2010.03.020.

[30] C. H. Ortiz, E. Hernandez-Rengifo, A. Guerrero, W. Aperador, and J. C. Caicedo, "Mechanical and Tribological Properties Evolution of [Si3N4/Al2O3]n Multilayer Coatings," *Tribology in Industry*, vol. 43, no. 1, pp. 23–39, Mar. 2021, doi: 10.24874/ti.952.08.20.01.

[31] B. Peng *et al.*, "High-temperature thermal stability and oxidation resistance of Cr and Ta co-alloyed Ti – Al – N coatings deposited by cathodic arc evaporation," *Corrosion Science*, vol. 167, p. 108490, Jan. 2020, doi: 10.1016/j.corsci.2020.108490 .

[32] G. Li *et al.*, "The performance of TIALSIN coated cemented carbide tools enhanced by inserting TI interlayers," *Metals*, vol. 9, no. 9, p. 918, Aug. 2019, doi: 10.3390/met9090918.

[33] F. Zhao, Z. Zhu, J. Yu, Z. Luo, and H. Qi, "Contrast Role of third body layer and hard abrasives in the wear process of a TIALSIN Hardness-Modulated Multilayer coating: A Case study on the effect of normal load and Velocity," *Coatings*, vol. 14, no. 7, p. 821, Jul. 2024, doi: 10.3390/coatings14070821.

[34] J. Liu *et al.*, "High-Temperature oxidation and wear resistance of TIALSIN/ALCRN multilayer coatings prepared by Multi-Arc Ion Plating," *Nanomaterials*, vol. 15, no. 7, p. 503, Mar. 2025, doi: 10.3390/nano15070503.

Article in Press

[35] Z. Wu, G. Zheng, J. Yan, X. Cheng, H. Liu, and X. Yang, "Effect of TiAlSiN coating residual stress on its sliding wear and cutting wear performance," *The International Journal of Advanced Manufacturing Technology*, vol. 123, no. 11–12, pp. 3885–3900, Nov. 2022, doi: 10.1007/s00170-022-10508-5.

[36] A. E. Reiter, V. H. Derflinger, B. Hanselmann, T. Bachmann, and B. Sartory, "Investigation of the properties of Al1−xCrxN coatings prepared by cathodic arc evaporation," *Surface and Coatings Technology*, vol. 200, no. 7, pp. 2114–2122, Apr. 2005, doi: 10.1016/j.surfcoat.2005.01.043.

[37] J. L. Endrino, G. S. Fox-Rabinovich, and C. Gey, "Hard AlTiN, AlCrN PVD coatings for machining of austenitic stainless steel," *Surface and Coatings Technology*, vol. 200, no. 24, pp. 6840–6845, Dec. 2005, doi: 10.1016/j.surfcoat.2005.10.030.

[38] A. F. O. Jiménez, H. S. Vanegas, C. M. Moreno, J. J. Olaya, and Y. Pineda, "The structural and mechanical properties of CRALTIN-SI nanostructured coatings deposited by the means of High-Power Impulse magnetron sputtering," *Metals*, vol. 13, no. 10, p. 1691, Oct. 2023, doi: 10.3390/met13101691.

[39] N. Panich, S. Surinphong, D. A. Karpov, Y. K. Tan, C. F. Goh, and J. Ma, "Mechanical properties of ALCRTISIN coatings developed by Cathodic Arc for protection applications," *State Phenomena*, vol. 185, pp. 81–83, Feb. 2012, doi: 10.4028/www.scientific.net/SSP.185.81.

[40] Y.-C. Kuo, C.-J. Wang, and J.-W. Lee, "The microstructure and mechanical properties evaluation of CrTiAlSiN coatings: Effects of silicon content," *Thin Solid Films*, vol. 638, pp. 220–229, Jul. 2017, doi: 10.1016/j.tsf.2017.07.058.

[41] *Standard Test Method for Linearly Reciprocating Ball-on-Flat Sliding Wear*, ASTM G133-05(2010), ASTM International, West Conshohocken, PA, USA, 2010, doi: 10.1520/G0133-05R10.

[42] J. F. Archard, "Contact and rubbing of flat surfaces," *Journal of Applied Physics*, vol. 24, no. 8, pp. 981–988, Aug. 1953, doi: 10.1063/1.1721448.

[43] W. C. Oliver and G. M. Pharr, "An improved technique for determining hardness and elastic modulus using load and displacement sensing indentation experiments," *Journal of Materials Research*, vol. 7, no. 6, pp. 1564–1583, Jun. 1992, doi: 10.1557/jmr.1992.1564.

[44] W. C. Oliver and G. M. Pharr, "Measurement of hardness and elastic modulus by instrumented indentation: Advances in understanding and refinements to methodology," *Journal of Materials Research*, vol. 19, no. 1, pp. 3–20, Jan. 2004, doi: 10.1557/jmr.2004.19.1.3.

[45] F. A. Estupiñan, C. M. Moreno, J. J. Olaya, and L. C. Ardila, "Wear resistance of TIALCRSIN coatings deposited by means of the Co-Sputtering technique," *Lubricants*, vol. 9, no. 6, p. 64, Jun. 2021, doi: 10.3390/lubricants9060064.

[46] J. Vetter, A. O. Eriksson, A. Reiter, V. Derflinger, and W. Kalss, "Quo vadis: ALCR-Based coatings in industrial applications," *Coatings*, vol. 11, no. 3, p. 344, Mar. 2021, doi: 10.3390/coatings11030344.

[47] A. Claver *et al.*, "Improved adhesion and tribological properties of ALTIN-TISIN coatings deposited by DCMS and HIPIMS on nitrided tool steels," *Coatings*, vol. 11, no. 10, p. 1175, Sep. 2021, doi: 10.3390/coatings11101175.

[48] N. Vidakis, A. Antoniadis, and N. Bilalis, "The VDI 3198 indentation test evaluation of a reliable qualitative control for layered compounds," *Journal of Materials Processing Technology*, vol. 143–144, pp. 481–485, Apr. 2003, doi: 10.1016/S0924-0136(03)00300-5.

[49] M. I. Aleutdinova and V. V. Fadin, "On the Probability of Melting on Sliding Surface of AISI 1020 Steel in Dry Sliding Against Quenched AISI 1045 Steel Under Electric Current," *Tribology in Industry*, vol. 48, no. 2, pp. 263–273, Mar. 2026, doi: 10.24874/ti.2056.10.25.01.

[50] K. Dohda, T. Aizawa, T. Funazuka, P. Soranansri, and K. Okamoto, "Designs and applications of nitride coatings to hot metal forming dies," *Friction*, vol. 14, no. 11, p. 9441248, Apr. 2026, doi: 10.26599/FRICT.2026.9441248.

[51] M. Kandeva, D. Karastoyanov, G. Nikolcheva, B. Stojanovic, P. Svoboda, and A. Vencl, "Tribological studies on copper-based friction linings," *Tribology in Industry*, vol. 39, no. 2, pp. 228–237, Jun. 2017, doi: 10.24874/ti.2017.39.02.10.

[52] R. Zhang, Q. Wang, Y. Xu, L. Li, and K. H. Kim, "Fabrication and properties of hard coatings by a hybrid PVD method," *Lubricants*, vol. 13, no. 9, p. 390, Sep. 2025, doi: 10.3390/lubricants13090390.

[53] R. H. Purba, D. I. Khoirunas, and K. Kusumoto, "Finite Element Analysis on Abrasive Wear Behavior of SKD 11 Tool Steel with Ti and Cr Based Hard Coatings: Material Selections," *Tribology in Industry*, vol. 48, no. 2, pp. 211–221, Mar. 2026, doi: 10.24874/ti.2048.10.25.12.

[54] J.-F. Tang, C.-Y. Lin, F.-C. Yang, and C.-L. Chang, "Influence of nitrogen content and bias voltage on residual stress and the tribological and mechanical properties of CRALN films," *Coatings*, vol. 10, no. 6, p. 546, Jun. 2020, doi: 10.3390/coatings10060546.

Article in Press